Efficient Optimization of Electron/Oxygen Pathway by Constructing Ceria/Hydroxide Interface for Highly Active Oxygen Evolution Reaction

Jiale Xia[+], Mingzi Sun[+], Hongyang Zhao[+], Bolong Huang*, Lingling Xu, Meng Luo, Jianwei Zhang, Feng Luo, Yaping Du*, and Chun-Hua Yan

J. Xia, H. Zhao, L. Xu, M. Luo and J. Zhang
Frontier Institute of Science and Technology, Xi'an Jiaotong University, Xi'an, Shaanxi 710054, China

M. Sun and Prof. B. Huang
Department of Applied Biology and Chemical Technology, The Hong Kong Polytechnic University, Hung Hom, Kowloon, Hong Kong SAR, 99907 China
bhuang@polyu.edu.hk

Prof. F. Luo
Instituto Madrileno de Estudios Avanzados en Nanociencia (IMDEA Nanociencia), Ciudad Universitaria de Cantoblanco, E-28049, Madrid, Spain

Prof. Y. Du and Prof. C.-H. Yan
School of Materials Science and Engineering & National Institute for Advanced Materials, Key Laboratory of Advanced Energy Materials Chemistry, Tianjin Key Lab for Rare Earth Materials and Applications, Centre for Rare Earth and Inorganic Functional Materials, Nankai University, Tianjin 300350, China
ypdu@nankai.edu.cn

Prof. C.-H. Yan
Beijing National Laboratory for Molecular Sciences, State Key Laboratory of Rare Earth Materials Chemistry and Applications, PKU-HKU Joint Laboratory in Rare Earth Materials and Bioinorganic Chemistry, College of Chemistry and Molecular Engineering, Peking University, Beijing 100871, China
and
College of Chemistry and Chemical Engineering, Lanzhou University, Lanzhou 730000, China

Keywords: Rare Earth Oxide, Oxygen Evolution Reaction, Noble Metal-free Electrocatalyst, Density Functional Theory, Core-shell Nanotube

Owing to the unique electronic properties, rare-earth modulations in noble-metal electrocatalysts emerge as a critical strategy for a broad range of renewable energy solutions such as water-splitting and metal-air batteries. Beyond the typical doping strategy that suffers from synthesis difficulties and the concentration limitations, the innovative introduction of rare-earth is highly desired. Here in this work, we present the novel synthesis strategy by introducing CeO_2 support for the Nickel-Iron-Chromium hydroxide (NFC) supported to boost the OER performance, which achieves an ultra-low overpotential at 10 mA/cm^2 of 230.8 mV, the Tafel

slope of 32.7 mV/dec as well as the excellent durability in alkaline solution. DFT calculations proved the established *d-f* electronic ladders by the interaction between NFC and CeO_2 evidently boosted the high-speed electron transfer. Meanwhile, the stable valence state in CeO_2 preserves the high electronic reactivity for OER. This work demonstrates a promising approach in fabricating the non-precious OER electrocatalyst with facilitation of rare-earth oxides to reach both excellent activity and high stability.

Due to global warming and fossil energy shortage issues, significate concerns have been given rise to the developing of renewable energy technologies.[1] Water splitting is considered as one of the most promising ways to generate hydrogen fuels for clean and sustainable energy demand. Oxygen evolution reaction (OER) is regarded as the bottleneck half-reaction for water splitting due to its sluggish kinetics compared with the hydrogen evolution reaction (HER), which usually requires a high overpotential as the driven force.[2] To overcome such a challenge, great effort has been devoted to exploring efficient and robust OER electrocatalysts. Presently, the precious metal Ir and Ru based materials have been considered as the benchmark materials for OER while the high cost greatly hinders their further commercialization in large-scale applications.[3] As alternative selections, the earth-abundant electrocatalysts with prominent activity and stability have attracted tremendous attention.[4] Recently the transition metal hydroxides are becoming potential candidates for OER due to their extraordinary electroactivity to OER as well as the low cost. [5] To further enhance their performance, the design strategies of the earth-abundant OER catalysts can be summarized in two aspects: one is tuning the catalyst electronic structures to optimize the intrinsic catalytic activity for fast electron transfer;[5a,6] the other is the structural engineering to facilitate the kinetics by modifying the local environment of catalyst surface.[7] Based on the rational design of nanocomposite catalysts, the realization of these two cooperative strategies will be able to achieve due to the unique interaction between nanoscale materials. On one hand, the electronic structure of catalyst can

be elaborately tuned by substrate species.[8] On the other hand, nanostructures can ameliorate the contact angle at gas/solid interfaces or expose more active sites to the electrolyte.[9] Also, nanocomposite catalyst can enhance the electrical conductivity by the unique small-size effect and nanostructure design.[10]

The structural engineering is playing a pivotal role in affecting the OER process regarding supplying more active sites, mechanical stability and oxygen releasement. When the view zoomed out at the nanoscale, the diffusion of oxygen species to catalyst becomes one of the dominant reasons to control the kinetics of OER due to the chemical equilibrium between reactants (oxygen-containing-intermediates) and product (O_2). These features will guarantee the efficient OER process under high current conditions for industrial applications. Recently, Liu's group reported that generating the lattice strain of NiFe hydroxide can effectively enhance the binding strength between NiFe hydroxide and oxygenated intermediates.[11] From another side, electronic engineering is also crucial to enhance the electrocatalytic performance. Through different doping selections, defect engineering and interfacial coupling effect, the intrinsic activity will be improved. Recent works have introduced ceria (CeO_x) to tradition catalysts for enhanced OER activity, benefiting from its excellent electronic/ionic conductivity and high oxygen-storage capacity. Mullins's group promoted the OER activity of CoO_x by introducing CeO_x and found that Ce promotes effective formation to CoOOH by perturbing the electronic structures of surface Co species.[12] Li's group developed high efficient FeOOH@CeO_2 heterolayered nanotube electrocatalysts for OER, the strong interactions between CeO_2 and FeOOH obviously lowers energy barriers for adsorptions of intermediates and products.[13] In addition, the CeO_x layer can also improve the durability of electrocatalysts due to its unique permselectivity, which allowing the permeation of OH* and O_2 through while preventing the diffusion of redox ions between electrolyte and electrode, thus ensure the long-term stability of the catalysts.[14]

In this work, we demonstrated the synergic design of highly catalytic NiFeCr hydroxide coated on oxygen permissive CeO_2 hollow nanotube with metallic copper core shows exceptionally high activity towards OER. First, we constructed the peapod-like Cu@CeO_2 nanotube array on Cu foam as the substrate through Ce^{3+} exchange with different concentration (0.10, 0.25, 0.50 and 1.00 mM) and subsequent annealing treatment under reducing atmosphere (denoted as Cu@CeO_2-x, x=0.10, 0.25, 0.50, 1.00). Next, the NiFeCr hydroxide nanosheets were deposited on the as-prepared substrate through the chronoamperometry measurement (denoted as Cu@CeO_2@NFC-x, x=0.10, 0.25, 0.50, 1.00). The introduction of CeO_2 substrate will simultaneously boost the oxygen ion transportation to the catalytic center and efficiently modulate the electronic structure of NiFeCr hydroxide for an energetically favorable state to accomplish water oxidation under alkaline environment. The excellent durability of the Cu@CeO_2@NFC electrocatalyst is also verified. Meanwhile, the copper core in the tubular structure offered high electric conductivity, which can benefit the fast electrons transport and leading to enhance OER activity. Distinct with conventional the Ce doping, DFT calculations confirmed that the CeO_2 supported layer supplied a broad range activation of the *d-f* coupling with the NFC that enriched active sites as well as the high charge transfer for O-species intermediates in OER. The energetically favorable reaction pathways are proved with an overpotential prediction close to the electrochemical tests. The conceptual illustration of catalyst design is depicted in **Figure 1**.

The morphologies of all samples were characterized by transition electron microscope (TEM), high-resolution transition electron microscope (HRTEM) and scanning electron microscope (SEM). It can be observed that after Ce^{3+} ion exchange, the Ce: $Cu(OH)_2$ nanorod shows similar smooth cylindric morphology to pristine $Cu(OH)_2$ nanorod with a uniform diameter of ~ 200 nm (**Figure S1**). The obtained Cu@CeO_{2-x} shows a core-shell structure and still

homogeneously grown on the Cu foam after reduction procedure (**Figure 2a**), while the $Cu(OH)_2$ nanorod exhibits a twisted solid cylinder structure after reduction (denoted as Cu NR) (**Figure S2, S3**). The formation of core-shell structure can be ascribed to the nanoscale Kirkendall effect.[15] The optimized $Cu@CeO_2@NFC$-0.25 sample was chosen as the representation for the following analysis. The TEM image of $Cu@CeO_2$-0.25 shows that the closely connected porous Cu core was encapsulated by a mesoporous tube wall constructed by CeO_2 nanoparticles (**Figure 2b**). **Figure 2c** shows the HRTEM image of $Cu@CeO_2$-0.25 interface. The lattice fringe of 0.21 nm and 0.31 nm are attributed to the (111) crystal plane of Cu composites and CeO_2 nanoparticles, respectively. The corresponding STEM-EDX elements mapping of Cu and Ce elements also confirmed the porous Cu nanocomposites structure and uniformly distributed CeO2 shell structure (**Figure 2d**).

After the NiFeCr hydroxide electrodeposited on $Cu@CeO_2$-0.25 substrate, the double-layered core-shell structure was observed (**Figure 2e, 2f**). The porous structure of the nanoarray composite electrode provides a larger active surface area to facilitate the electrolyte penetration on both nanoscale and microscale. In addition, the vertical nanoarray structure will benefit the fast release of gas bubbles from the electrode surface, thus promoting the electronic transfer and leading to enhanced OER activity. [16] The interplanar distance of 0.18 nm, 0.19 nm and 0.31 nm in the HRTEM images well matched to the (200) crystal plane of Cu nanocomposites, (220) and (111) crystal of CeO_2 nanoparticles (**Figure 2g**). Besides, the unapparent lattice fringe found in this HRTEM image indicates the low crystallinity of NiFeCr hydroxide, which endows their excellent OER activity. It has been widely reported that metal oxides or hydroxides with low crystallinity or amorphous structure can provide more active sites due to the abundant surface defects and lattice dislocations, thus showing superior OER activity compared to their crystalline counterparts.[17] Notably, the obvious lattice junction between CeO_2 nanoparticles and NiFeCr hydroxide as well as the junction between CeO_2 wall and Cu

core, indicating their close interaction, which will provide a good charge transfer path to achieve the excellent electronic conductivity. The STM-EDX element mapping was also measured to demonstrate the uniformed coated CeO_2 and NiFeCr hydroxide multilayer structure (**Figure 2h**). After the long-time OER test, the Cu@CeO_2@NFC-0.25 can still maintain the core-shell structure (**Figure S4**), indicating its excellent morphological stability. The indistinct lattice fringe in HRTEM image indicated the subcrystalline structure of NiFeCr hydroxides, which is consistent with the results before. The low crystallinity of NFC can also been confirmed by the Raman spectra that no obvious signals was detected (**Figure S5**). X-ray diffraction (XRD) characterization was carried out to measure the structure of the samples. As **Figure S6** shows, the XRD patterns of Cu NR substrate, Cu@CeO_2-0.25 substrate and Cu@CeO_2@NFC-0.25 before and after OER test follows the typical diffraction peaks of Cu. The absence of characteristic diffraction peaks of NFC and CeO_2 can be ascribed to the low crystallinity of NFC and low contents of CeO_2 nanoparticles, which match well with the results above.

X-ray photoelectron spectroscopy (XPS) measurements were employed to further investigate the surface chemical compositions and valence states of Cu@CeO_2@NFC-0.25 before and after OER test. As shown in **Figure 3a**, the Cu@CeO_2@NFC-0.25 before OER test shows typical Ni 2p peaks at 855.7 eV and 873.3 eV, which is corresponded to Ni $2p_{3/2}$ and $2p_{1/2}$ of Ni^{2+}, respectively.[18] Similarly, the co-existence of Fe and Cr are proved as well. The spectra peaks of Fe $2p_{1/2}$ and $2p_{3/2}$ are located at 711.4 eV and 724.0 eV respectively, which can be indexed to Fe^{3+} of $Fe(OH)_3$ (**Figure 3b**).[19] The slight separation of Fe $2p_{1/2}$ and $2p_{3/2}$ peaks after OER was possibly due to the local chemical environment change induced by nickel oxidation. This result match well with earlier reports about NiFe LDHs materials, confirming the composition of NiFe based hydroxide as well as the oxidation state of Ni^{2+} and Fe^{3+} in this composite. [20] In addition, the Cr 2p spectra located at 576.5 eV and 578.2 eV are related to Cr^{3+}-O and Cr^{3+}-OH respectively (**Figure 3c**). The decrease of relative intensity ration of Cr^{3+}-OH peaks could be a

result of strong oxidation condition during the OER measurements changed Cr^{3+}-OH to Cr^{3+}-O.[21] Moreover, when it comes to O 1s spectra in Figure 3d, the simulated peaks located at 529.3 eV, 531.0 eV and 532.1 eV were assigned to M-O, M-OH and H_2O, respectively.[22] Besides, the relative intensity ratio of M-O and H_2O peaks increased obviously after long-time OER test, which is consistent with the XPS results above. For Ce 3d spectra, there are three sets of peaks of Cu@CeO_2-0.25 substrate (**Figure S7**). The peaks located at 882-890 eV and 898-920 eV were corresponded to Ce $3d_{3/2}$ and Ce $3d_{5/2}$ respectively, which showed the coexistence of Ce^{3+} and Ce^{4+}, indicating the multivalence property of ceria. It can be seen that Ce 3d signal became insignificant after OER process, indicating the leaching of cerium. After the NFC deposition, the molar ratio of Ce^{3+}/Ce^{4+} increased significantly, indicating the close interaction between CeO_2 and NFC. Furthermore, the slight change of Ce^{3+}/Ce^{4+} molar ration after long-time OER test is ascribed to the charge transfer between NFC and CeO_2 during the OER process. Compared with Cu@CeO_2-0.25 substrate, the Ce 3d signal remained unchanged for NFC coated samples after OER process. This indicated that NFC coating stablized CeO_2 layer during strong oxidation conditions. Notably, the similar peak positions of Ni, Fe, Cr and Ce before and after long-time OER test indicated the excellent chemical stability of the trimetallic hydroxide system during OER measurements.

The electrocatalytic OER performances of Cu@CeO_2@NFC electrocatalysts were firstly optimized by adjusting the concentration of CeO_2. Here, we developed four samples with different CeO_2 ratio of Cu@CeO_2@NFC-x (x=0.1, 0.25, 0.5, 1.0). As shown in **Figure S7**, the Cu@CeO_2@NFC-0.25 shows the highest OER activity in terms of the lowest overpotential and lowest Tafel slope. When the Ce^{3+} reaction concentration increases from 0.1 mM to 0.25 mM, the overpotential at 10 mA/cm^2 decreases from 245.9 to 230.8 mV, with the Tafel slope decreases from 50.9 to 32.7 mV/dec simultaneously. The improved OER activity can be originated from the enhanced electron transfer and oxygen transfer capability induced by the

increased CeO_2 concentration. With the further increase of Ce^{3+} concentration to 0.5 mM and 1.0 mM, the OER activity gradually decreases. When the Ce^{3+} concentration reached 1.0 mM, the overpotential at 10 mA/cm^2 and Tafel slope were 243.9 mV and 54.6 mV/dec, respectively. The degradation of OER activities at high concentration of CeO_2 could result from the more scattered Cu nanocomposites, leading to the reduced electrical conductivity of the Cu@CeO_2 substrate.

To further investigate the structure influence on the OER activity, the Cu foam and the as-prepared Cu NR were employed as the substrates for NiFeCr hydroxide electrodeposition for comparison. The obtained samples were denoted as CNR@NFC and CF@NFC, respectively. As the polarization curves are shown in **Figure 4a**, the bare Cu@CeO_2-0.25 substrate shows a negligible OER current within the potential range. We can see that Cu@CeO_2@NFC-0.25 exhibits a much lower onset potential and much higher catalytic current density compared with other samples. The overpotential (η) at the current density of 10 mA/cm^2 of Cu@CeO_2@NFC-0.25 is merely 230.8 mV, which is lower than 233.4 mV of commercial RuO_2 and far below 252.8 mV and 256.1 mV of CNR@NFC and CF@NFC, respectively. The Tafel slopes were also calculated by plotting the overpotential against log (j) from corresponding polarization curves to get further insight into the OER kinetics (**Figure 4b**). From the summaries in **Figure 4c**, the Tafel slope of Cu@CeO_2@NFC is 32.7 mV/dec, which is far below 58.1 mV/dec, 83.0 mV/dec and 87.4 mV/dec corresponding to CNR@NFC, CF@NFC and commercial RuO_2. The significantly lower Tafel slope indicates the better OER kinetics of Cu@CeO_2@NFC, which can be owing to the vertical Cu nanowire array structure on Cu foam, not only enlarge the electrochemically active surface but also facilitate the gas bubble release on the electrode surface. Moreover, the excellent electronic/ionic conductivity and high oxygen storage capacity of CeO_2 are also beneficial to the enhancement of the OER reaction kinetics.

Moreover, the excellent steady-state activity of Cu@CeO_2@NFC was evidenced by the multi-current step chronopotentiometric measurement in 1 M KOH with the current density increased from 10 mA/cm^2 to 500 mA/cm^2. As **Figure 4d** shows, the overpotential immediately reached 232 mV at an initial applied current density of 10 mA/cm^2 and almost remained the same in the following 1 h with no observation of evident fluctuations. With the increase of current density steps, the overpotential increased and maintained an identical level. Mentionable, the overpotential shows negligible fluctuation even at 100 mA/cm^2 or higher current density, which is beneficial from the fast oxygen releasement *via* the vertical core-shell nanowire structure. In addition, the chronopotentiometric test was further conducted at the current density of 10 and 20 mA/cm^2 for a long-time period to characterize the long-term stability of Cu@CeO_2@NFC-0.25 electrocatalyst. Notably, the overpotential was stable at 236 mV for 12 h at 10 mA/cm^2. Similar results were also detected at the applied current density of 20 mA/cm^2 with the stabilized overpotential at 276 mV (**Figure 4e**), indicating the excellent durability of Cu@CeO_2@NFC-0.25 electrocatalyst in alkaline solution. These results confirmed the excellent charge transfer, fast gas releasement and long-term durability of the Cu@CeO_2@NFC-0.25 hybrid electrocatalyst.

The introduction of CeO_2 does not only serve as a fast electron transfer path but also greatly affect the structure. The electrochemical surface area (ECSA) was estimated from the double-layer capacitance (C_{dl}) of Cu@CeO_2@NFC-x, CNR@NFC and CF@NFC by measuring the charging current in a potential window free of Faradaic process (**Figure S9, S10**). As shown in **Figure 5a**, the linear slope of Cu@CeO_2@NFC-0.25 was calculated to be 2.74 mF/cm^2, which is much higher than the value of 1.73 mF/cm^2 and 0.62 mF/cm^2 corresponding to CNR@NFC and CF@NFC, respectively. The much higher C_{dl} value of Cu@CeO_2@NFC-0.25 is attributed to the large active surface area due to the porous nanotube array structure, which is in accordance with the OER activity. As oxygen anion diffusion rate is an important influential

factor on the OER process, better oxygen ion diffusion would significantly improve the electrochemical kinetics.[23] In order to study the oxygen ion diffusion behavior of the prepared electrodes, chronoamperometric measurements were carried out as to calculate the diffusion coefficients *D*. According to the bounded three-dimensional diffusion model theory,[24] the diffusion coefficients *D* has remarkably increased due to the CeO_2 incorporation (**Figure 5b, S11, Table 1**). Compared to the CF@NFC, the ion diffusion coefficient has enlarged more than two times, indicating the significant improved ion diffusion speed. Moreover, the ion diffusion coefficient has increased as the concentration of CeO_x due to the efficient oxygen storage and release speed, which further supports our motivation of applying CeO_x to facilitate the OER performance.

The electrochemical impedance spectroscopy (EIS) matched well with the above measurements on diffusion coefficients. As shown in **Figure 5c**, all the samples exhibited compressed semicircles that correlated to the OER kinetics. When applied the corresponding potential at 10 mA/cm^2, the EIS plot Cu@CeO_2@NFC showed a much smaller semicircle diameter than CNR@NFC and CF@NFC, indicating the superior charge-transfer rate and electronic conductivity. Furthermore, EIS at a different applied potential increase from 0.45 to 0.6 V vs. Ag/AgCl with an increased range of 0.025 V was shown in **Figure 5d** and **Figure S12**. It can be observed that all the catalyst electrodes show similar variation tendency of both charge transfer resistance (R_{ct}) and solution resistance (R_s). When the applied potential increased stepwise to 0.55 V, Cu@CeO_2@NFC-0.25 showed less charge transfer resistance than other samples, indicating its better charge transfer capability. The gradually decreased R_{ct} with the increased applied potential can be related to the intensified OER process. In the meantime, the R_s of all the samples show little difference and almost remain the same during this process. When the applied potential was larger than 0.55 V, the R_{ct} of all the samples has a slight increase while the R_s values increase more rapidly. The larger R_s of Cu@CeO_2@NFC can be ascribed

to the formation of insulating gas bubble layer within the more drastic OER process, illustrating a superior OER activity of Cu@CeO_2@NFC. Concurrently, the R_{ct} of Cu@CeO_2@NFC at high applied potential is stabilized by the fast gas bubbles releasing from the porous nanotube array aligned structure.

To unveil the critical role of CeO_2 to enhance the OER on pristine Cu@NFC, we have performed theoretical calculations from both electronic and energetic perspectives. The projected partial density of states (PDOS) of O-2p orbitals in the NFC layer and CeO_2 have been presented with very distinct electronic behaviours (**Figure 6a, b**). The NFC layer displayed mobile O-2p orbitals, in which the dominant peak of O-2p gradually migrated from 4 eV below Fermi level (E_F) to 6 eV below E_F. On the contrary, CeO_2 exhibited a pinned electronic position of O-2p orbitals that distributed at a higher position between E_F-5 eV and E_F-1 eV during OER that further lead to a stable valence state of Ce in the bottom CeO_2 layer. With the introduction of CeO_2, the electronic orbital distribution near E_F has largely enriched. The large barriers between the common d-d bands have been alleviated to subtle gaps by both the Ce-4f orbitals and 3d orbitals from Fe/Cr dopants (**Figure 6c**). The widely distributed orbitals covered the range from E_F-2 eV E_F+4 eV, indicating a highly efficient "electron transfer expressway" by the formation of *d-f* electronic ladders. Such *d-f* electronic ladders still stably existed with slight change during the OER (**Figure S13**). Leveraging on the pinned O-2p orbitals in CeO_2, Ce-4f orbitals show occupation below E_F that remained nearly unchanged, supporting the reduced valence state of Ce atoms with high electrocatalytic reactivity. The 3d orbitals of Ni, Fe and Cr are well-matched covering a large range, which demonstrated a good electron transfer based on solid bonding. The integral migration of 3d orbitals during the OER also proved that origins of high reactivity near the "3d-unit" (Ni, Fe and Cr). Moreover, the mobile O-2p position of the NFC hydroxide is following the O-2p from O-species adsorbates. The weak overlap between the surface [OH] groups and the metal will easily result in the

unsaturation of surface bonding to expose more active sites for OER. The similar trend of O-2p in NFC with the adsorbates O-2p demonstrated a potential "matter exchange" mechanism between the surface [OH] groups and the reaction intermediates, which will further enhance the OER by the matter-accelerated reactions. Beyond the Ce doping method, the additional CeO_2 layer played a pivotal role in the facilitation of the OER by supplying a high-speed charge transfer pathway for electron delocalization. Beneficial from the protection of the pinned O-2p orbitals, a stable electronic valence state of Ce also ensured the high electrocatalytic reactivity.

The surface configuration of the important adsorbates during OER are in a good agreement with the potential "matter exchange" mechanism (**Figure 6d**). The highly disordered NFC surface demonstrates loose bondings of surface [OH] groups, which expose the active sites with strong water-splitting capability, supporting the amorphous structure experimental observations. Notably, all the adsorbates have been stabilized near the "3d orbitals triangle", which is consistent with the previous electronic properties. The coupling between Ce-4f and NFC-3d units supplied the highly active sites for a fast charge transfer that can proceed with the OER process. The advantages of CeO_2 are further revealed from the energetic perspectives (**Figure 6e**). The initial dissociation of H_2O on NFC-CeO_2 exhibited evident superior energy of 1.52 eV than that of the pristine NFC system with a massive energy barrier of 2.54 eV. Thus, the overpotential has been determined as 0.29 V by the largest barrier of the reaction path, which is very close to the experiment results. Though the formation of [*O] is energetically favorable on NFC, the following energy gap will largely constrain the OER efficiency. Moreover, the barrier of the potential rate-determining step in forming [*OOH] during OER has been attenuated to 1.17 eV in NFC-CeO_2 system while the pure NFC confronted a large energy barrier of 2.68 eV. Thus, the benefits of the high electron pathway by the assistance of CeO_2 is also reflected by the overall energetic pathway of OER. Here in this work, we have proposed the significance of CeO_2 layer in boosting the OER process by the formation of "*d-f* electronic

ladders" as a charge transfer highway (**Figure 6f**). Distinct with the normal Ce doping, the O-2p orbitals from the oxide layer provided good protection for maintaining the low valence state of Ce that contributed to the "*d-f* electronic ladders". The efficient electron transfer is achieved through diving to the Ce-4f orbitals and bounced back to the NFC layer through the acceleration of the charge transfer highway based on the strong *d-f* coupling. Therefore, such Cu@CeO_2@NFC system is a promising electrocatalyst for the OER process.

In summary, we have demonstrated a novel and highly efficient hybrid electrocatalyst composed of NiFeCr hydroxide deposited on porous peapod-like Cu@CeO_2 nanotube array. In an alkaline environment, the durable Cu@CeO_2@NFC-0.25 exhibits excellent OER catalytic performance with low overpotential at 10 mA/cm^2 of 230.83 mV and Tafel slope of 32.7 mV/dec. Theoretical calculations confirmed the introduction of CeO_2 will significantly enrich the electronic distribution near E_F, supplying a springboard to largely enhance the electron transfer efficiency from local Cu@CeO_2@NFC-0.25 to adsorbates. The superior OER performance will be ascribed to the synergic optimization of the local structures and electronic environments including large ECSA with sufficient active sites, nanoarray structures for quick oxygen diffusion and releasement, and the *d-f* orbital coupling for great promoted electron transfer. The obtained Cu@CeO_2@NFC catalysts exhibit remarkable OER catalytic activity and superior long-term stability compared to the state-of-art RuO_2 catalyst, thus providing a promising way for the design of highly activity novel noble-metal-free OER catalyst.

Supporting Information
Supporting Information is available from the Wiley Online Library or from the author.

Acknowledgements
Research reported in this publication were supported by the China National Funds for Excellent Young Scientists (grant no. 21522106) and the National Key R&D Program of China (2017YFA0208000), the Natural Science Foundation of China (21771156), and the Early Career Scheme (ECS) fund (Grant No.: PolyU 253026/16P) from the Research Grant Council

(RGC) in Hong Kong. We thank the Instrument Analysis Center of Xi'an Jiaotong University for their assistance on characterizations. J. Xia, M. Sun and H. Zhao contribute equally to this work.

Received: ((will be filled in by the editorial staff))
Revised: ((will be filled in by the editorial staff))
Published online: ((will be filled in by the editorial staff))

References

[1] a) D. Larcher, J. M. Tarascon, *Nat. Chem.* **2015**, 7, 19; b) S. Chu, A. Majumdar, *Nature* **2012**, 488, 294; c) S. Chu, Y. Cui, N. Liu, *Nat. Mater.* **2016**, 16, 16.
[2] a) N. T. Suen, S. F. Hung, Q. Quan, N. Zhang, Y. J. Xu, H. M. Chen, *Chem. Soc. Rev.* **2017**, 46, 337; b) L. C. Seitz, C. F. Dickens, K. Nishio, Y. Hikita, J. Montoya, A. Doyle, C. Kirk, A. Vojvodic, H. Y. Hwang, J. K. Norskov, *Science* **2016**, 353, 1011.
[3] A. Di Blasi, C. D'urso, V. Baglio, V. Antonucci, R. Ornelas, F. Matteucci, G. Orozco, D. Beltran, Y. Meas, L. Arriaga, *J. Appl. Electrochem.* **2009**, 39, 191.
[4] a) I. Roger, M. A. Shipman, M. D. Symes, *Nat. Rev. Chem.* **2017**, 1, 0003; b) B. M. Hunter, H. B. Gray, A. M. Muller, *Chem. Rev.* **2016**, 116, 14120.
[5] a) J. Jiang, F. Sun, S. Zhou, W. Hu, H. Zhang, J. Dong, Z. Jiang, J. Zhao, J. Li, W. Yan, M. Wang, *Nat. Commun.* **2018**, 9, 2885; b) F. Dionigi, P. Strasser, *Adv. Energy Mater.* **2016**, 6, 1600621.
[6] a) D. K. Bediako, B. Lassalle-Kaiser, Y. Surendranath, J. Yano, V. K. Yachandra, D. G. Nocera, *J. Am. Chem. Soc.* **2012**, 134, 6801; b) M. A. Lukowski, A. S. Daniel, F. Meng, A. Forticaux, L. Li, S. Jin, *J. Am. Chem. Soc.* **2013**, 135, 10274; c) H. Wang, Z. Lu, D. Kong, J. Sun, T. M. Hymel, Y. Cui, *ACS Nano* **2014**, 8, 4940; d) Y. Shi, Y. Zhou, D. R. Yang, W. X. Xu, C. Wang, F. B. Wang, J. J. Xu, X. H. Xia, H. Y. Chen, *J. Am. Chem. Soc.* **2017**, 139, 15479; e) S. H. Ye, Z. X. Shi, J. X. Feng, Y. X. Tong, G. R. Li, *Angewandte Chemie* **2018**, 57, 2672.
[7] a) T. Ling, D.-Y. Yan, Y. Jiao, H. Wang, Y. Zheng, X. Zheng, J. Mao, X.-W. Du, Z. Hu, M. Jaroniec, S.-Z. Qiao, *Nat. Commun.* **2016**, 7, 12876; b) C. Guo, Y. Zheng, J. Ran, F. Xie, M. Jaroniec, S. Z. Qiao, *Angew. Chem. Int. Ed.* **2017**, 56, 8539; c) Y. Zhu, L. Peng, Z. Fang, C. Yan, X. Zhang, G. Yu, *Adv. Mater.* **2018**, 30, 1706347; d) J. X. Feng, H. Xu, Y. T. Dong, S. H. Ye, Y. X. Tong, G. R. Li, *Angewandte Chemie* **2016**, 55, 3694; e) X. F. Lu, L. F. Gu, J. W. Wang, J. X. Wu, P. Q. Liao, G. R. Li, *Adv Mater* **2017**, 29.
[8] a) P. Chakthranont, J. Kibsgaard, A. Gallo, J. Park, M. Mitani, D. Sokaras, T. Kroll, R. Sinclair, M. B. Mogensen, T. F. Jaramillo, *ACS Catal.* **2017**, 7, 5399; b) S. Zou, M. S. Burke, M. G. Kast, J. Fan, N. Danilovic, S. W. Boettcher, *Chem. Mater.* **2015**, 27, 8011; c) D. Guo, J. Qi, W. Zhang, R. Cao, *ChemSusChem* **2017**, 10, 394.
[9] Z. Lu, W. Zhu, X. Yu, H. Zhang, Y. Li, X. Sun, X. Wang, H. Wang, J. Wang, J. Luo, X. Lei, L. Jiang, *Adv. Mater.* **2014**, 26, 2683.
[10] a) Z. Liu, Z. Yin, C. Cox, M. Bosman, X. Qian, N. Li, H. Zhao, Y. Du, J. Li, D. G. Nocera, *Sci. Adv.* **2016**, 2, e1501425; b) X. Liu, Z. Chang, L. Luo, T. Xu, X. Lei, J. Liu, X. Sun, *Chem. Mater.* **2014**, 26, 1889.
[11] D. Zhou, S. Wang, Y. Jia, X. Xiong, H. Yang, S. Liu, J. Tang, J. Zhang, D. Liu, L. Zheng, Y. Kuang, X. Sun, B. Liu, *Angew. Chem. Int. Ed.* **2019**, 58, 736.
[12] J.-H. Kim, K. Shin, K. Kawashima, D. H. Youn, J. Lin, T. E. Hong, Y. Liu, B. R. Wygant, J. Wang, G. Henkelman, C. B. Mullins, *ACS Catal.* **2018**, 8, 4257.
[13] J. X. Feng, S. H. Ye, H. Xu, Y. X. Tong, G. R. Li, *Adv. Mater.* **2016**, 28, 4698.
[14] K. Obata, K. Takanabe, *Angew. Chem. Int. Ed.* **2018**, 57, 1616.

[15] a) Y. Yin, R. M. Rioux, C. K. Erdonmez, S. Hughes, G. A. Somorjai, A. P. Alivisatos, *Science* **2004**, 304, 711; b) H. Jin Fan, M. Knez, R. Scholz, K. Nielsch, E. Pippel, D. Hesse, M. Zacharias, U. Gosele, *Nat. Mater.* **2006**, 5, 627; c) Y. Tang, S. Chen, S. Mu, T. Chen, Y. Qiao, S. Yu, F. Gao, *ACS Appl. Mater. Interfaces* **2016**, 8, 9721.
[16] Z. Lu, Y. Li, X. Lei, J. Liu, X. Sun, *Mater. Horiz.* **2015**, 2, 294.
[17] a) Y. Li, C. Zhao, *ACS Catal.* **2017**, 7, 2535; b) R. D. Smith, M. S. Prévot, R. D. Fagan, Z. Zhang, P. A. Sedach, M. K. J. Siu, S. Trudel, C. P. Berlinguette, *Science* **2013**, 340, 60; c) Y. Yang, H. Fei, G. Ruan, C. Xiang, J. M. Tour, *ACS Nano* **2014**, 8, 9518.
[18] a) X. Bo, Y. Li, R. K. Hocking, C. Zhao, *ACS Appl. Mater. Interfaces* **2017**, 9, 41239; b) M. A. Oliver-Tolentino, J. Vázquez-Samperio, A. Manzo-Robledo, R. d. G. González-Huerta, J. L. Flores-Moreno, D. Ramírez-Rosales, A. Guzmán-Vargas, *J. Phys. Chem. C* **2014**, 118, 22432.
[19] K. Yan, T. Lafleur, J. Chai, C. Jarvis, *Electrochem. Commun.* **2016**, 62, 24.
[20] a) Y. Hou, M. R. Lohe, J. Zhang, S. Liu, X. Zhuang, X. Feng, *Energy Environ. Sci.* **2016**, 9, 478; b) L. Yu, H. Zhou, J. Sun, F. Qin, F. Yu, J. Bao, Y. Yu, S. Chen, Z. Ren, *Energy Environ. Sci.* **2017**, 10, 1820; c) S. Anantharaj, K. Karthick, M. Venkatesh, T. V. Simha, A. S. Salunke, L. Ma, H. Liang, S. Kundu, *Nano Energy* **2017**, 39, 30.
[21] a) Y. Yang, L. Dang, M. J. Shearer, H. Sheng, W. Li, J. Chen, P. Xiao, Y. Zhang, R. J. Hamers, S. Jin, *Adv. Energy Mater.* **2018**, 8, 1703189; b) C. Dong, X. Yuan, X. Wang, X. Liu, W. Dong, R. Wang, Y. Duan, F. Huang, *J. Mater. Chem. A* **2016**, 4, 11292.
[22] H. Ali-Löytty, M. W. Louie, M. R. Singh, L. Li, H. G. Sanchez Casalongue, H. Ogasawara, E. J. Crumlin, Z. Liu, A. T. Bell, A. Nilsson, D. Friebel, *J. Phys. Chem. C* **2016**, 120, 2247.
[23] a) J. T. Mefford, X. Rong, A. M. Abakumov, W. G. Hardin, S. Dai, A. M. Kolpak, K. P. Johnston, K. J. Stevenson, *Nat. Commun.* **2016**, 7, 11053; b) Y. Liu, Z. Wang, J.-P. M. Veder, Z. Xu, Y. Zhong, W. Zhou, M. O. Tade, S. Wang, Z. Shao, *Adv. Energy Mater.* **2018**, 8, 1702604.
[24] a) E. Vago, E. Calvo, *J. Electroanal. Chem.* **1992**, 339, 41; b) F. Van Buren, G. Broers, C. Boesveld, A. Bouman, *J. Electroanal. Chem. Interfacial Electrochem.* **1978**, 87, 381; c) F. Van Buren, G. Broers, A. Bouman, C. Boesveld, *J. Electroanal. Chem. Interfacial Electrochem.* **1978**, 88, 353; d) F. Van Buren, G. Broers, A. Bouman, C. Boesveld, *J. Electroanal. Chem. Interfacial Electrochem.* **1978**, 87, 389.

Table 1. The normalized oxygen diffusion coefficients (*D*) of different samples.

Sample	CF@NFC	CNR@NFC	Cu@CeO_2@NFC-0.10	Cu@CeO_2@NFC-0.25	Cu@CeO_2@NFC-0.50	Cu@CeO_2@NFC-1.00
Normalized *D*	1	1.23	1.87	2.18	2.69	2.91

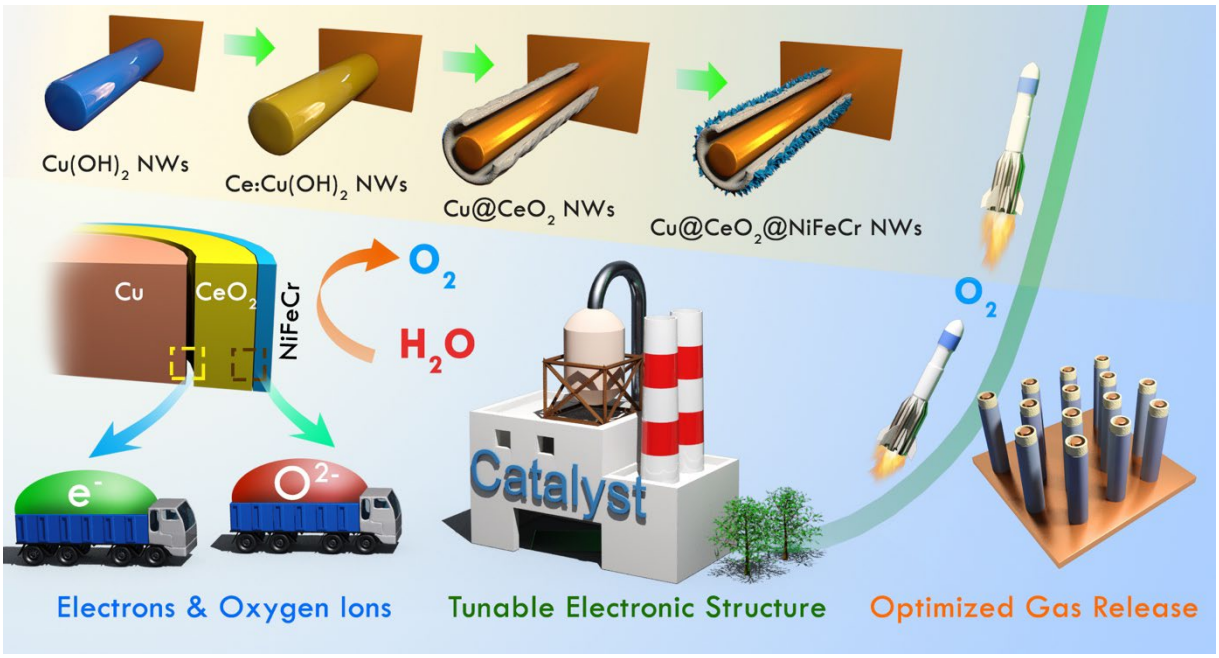

Figure 1. Schematic illustration of the design of Cu@CeO₂@NFC electrocatalysts.

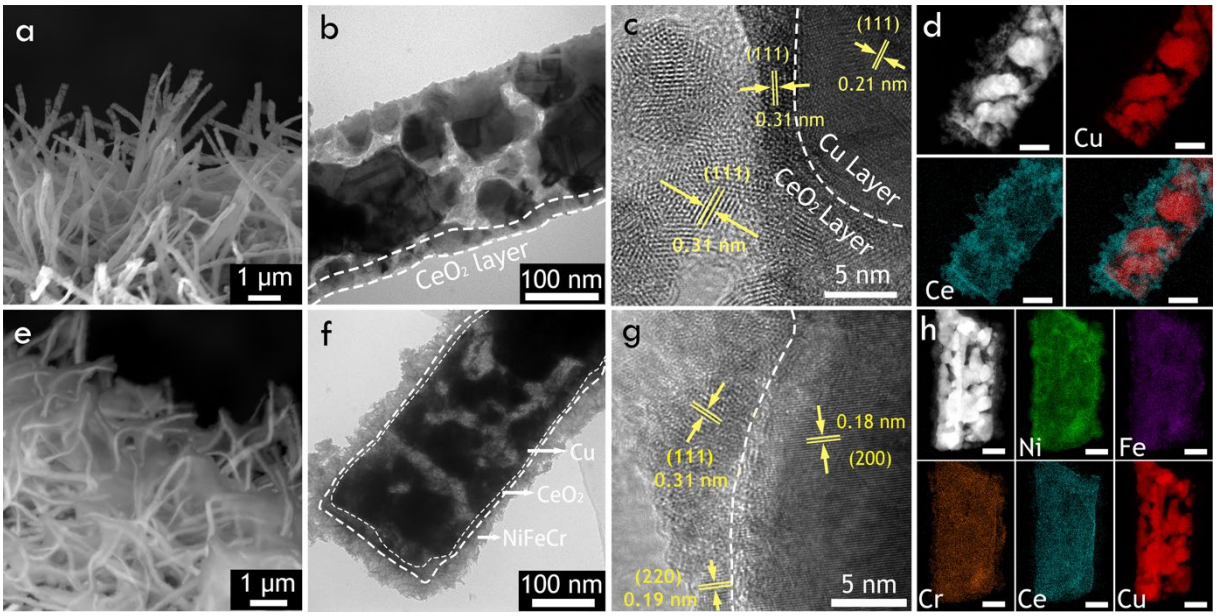

Figure 2. Structural characterizations of Cu@CeO₂@NFC electrocatalysts. (a) SEM image; (b) TEM image and (c) HRTEM image of Cu@CeO₂-0.25 substrate. (d) Annual dark-field TEM image of Cu@CeO₂-0.25 and corresponding EDX mapping of Ce and Cu elements. The scale bar = 100 nm. (e) SEM image; (f) TEM image and (g) HRTEM image of Cu@CeO₂@NFC-0.25 electrocatalyst; (h) Annual dark-field TEM image of Cu@CeO₂@NFC-0.25 and corresponding EDX mapping of Ni, Fe, Cr, Ce and Cu elements. The scale bar = 100 nm.

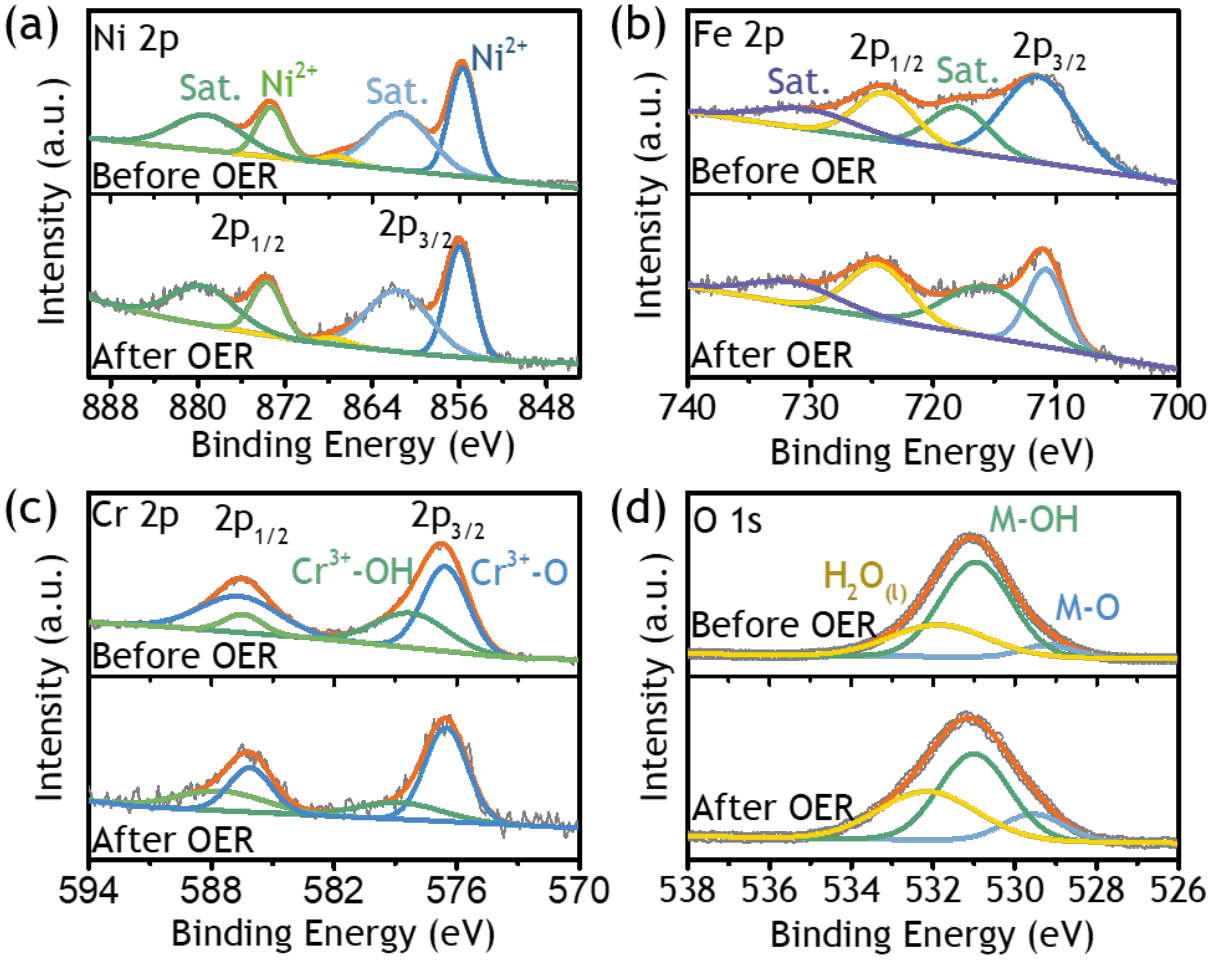

Figure 3. High-resolution XPS spectra of Cu@CeO₂@NFC-0.25 electrocatalyst before and after OER reaction. (a) Ni 2p. (b) Fe 2p. (c)Cr 2p. (d) O 1s.

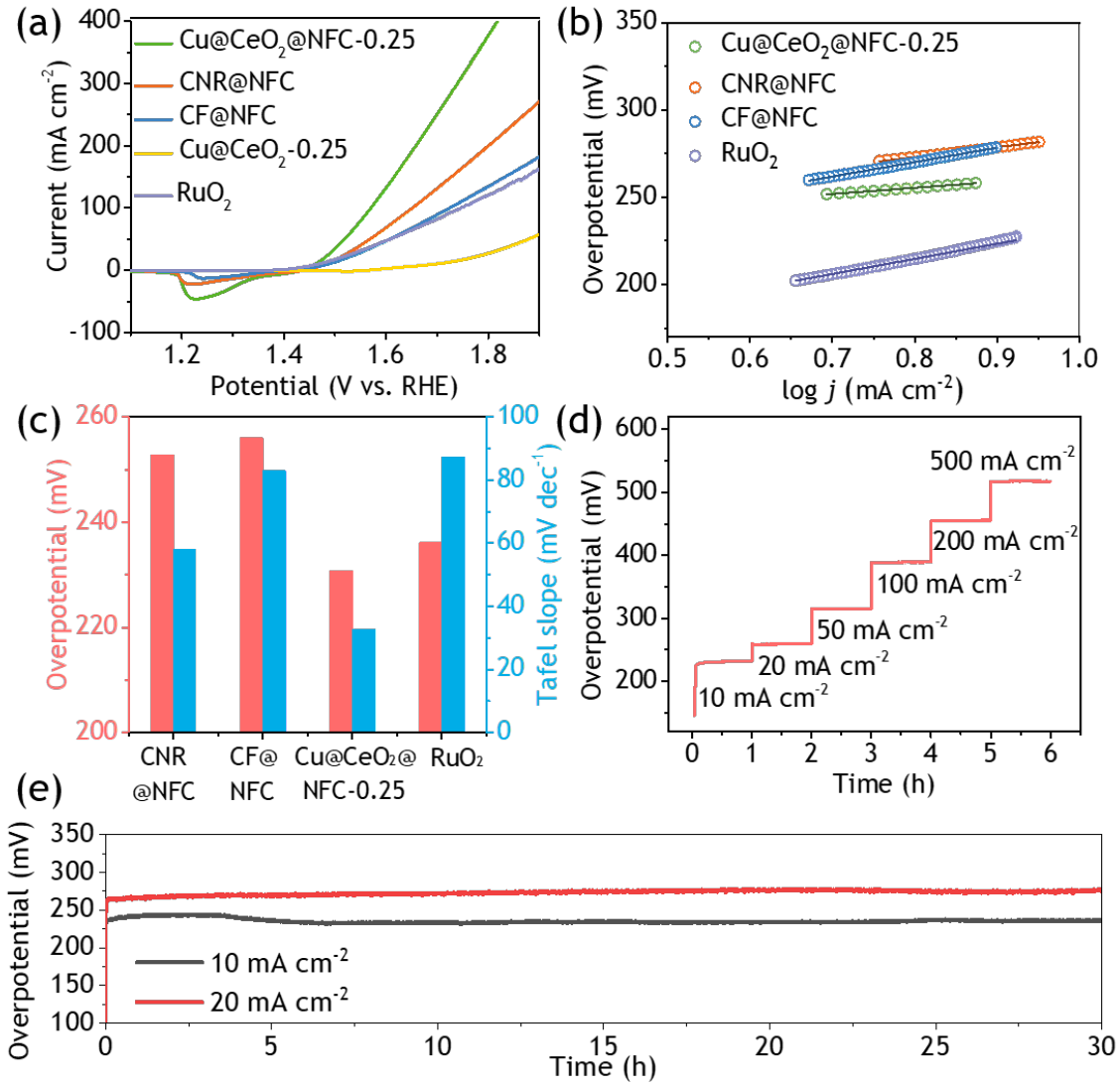

Figure 4. Electrocatalytic OER performances Comparison. (a) Polarization curves and (b) corresponding Tafel plots of CF@NFC, CNR@NFC, Cu@CeO_2@NFC-0.25 and commercial RuO_2. (c) Comparison of overpotential and Tafel slope of CNR@NFC, CF@NFC, Cu@CeO_2@NFC-0.25 and RuO_2. (d) Chronopotentiometric measurements of Cu@CeO_2@NFC-0.25 in 1.0 M KOH at various current densities; (e) Extended chronopotentiometric measurements at j = 10 mA cm^{-2} and j = 20 mA cm^{-2} for 30 h.

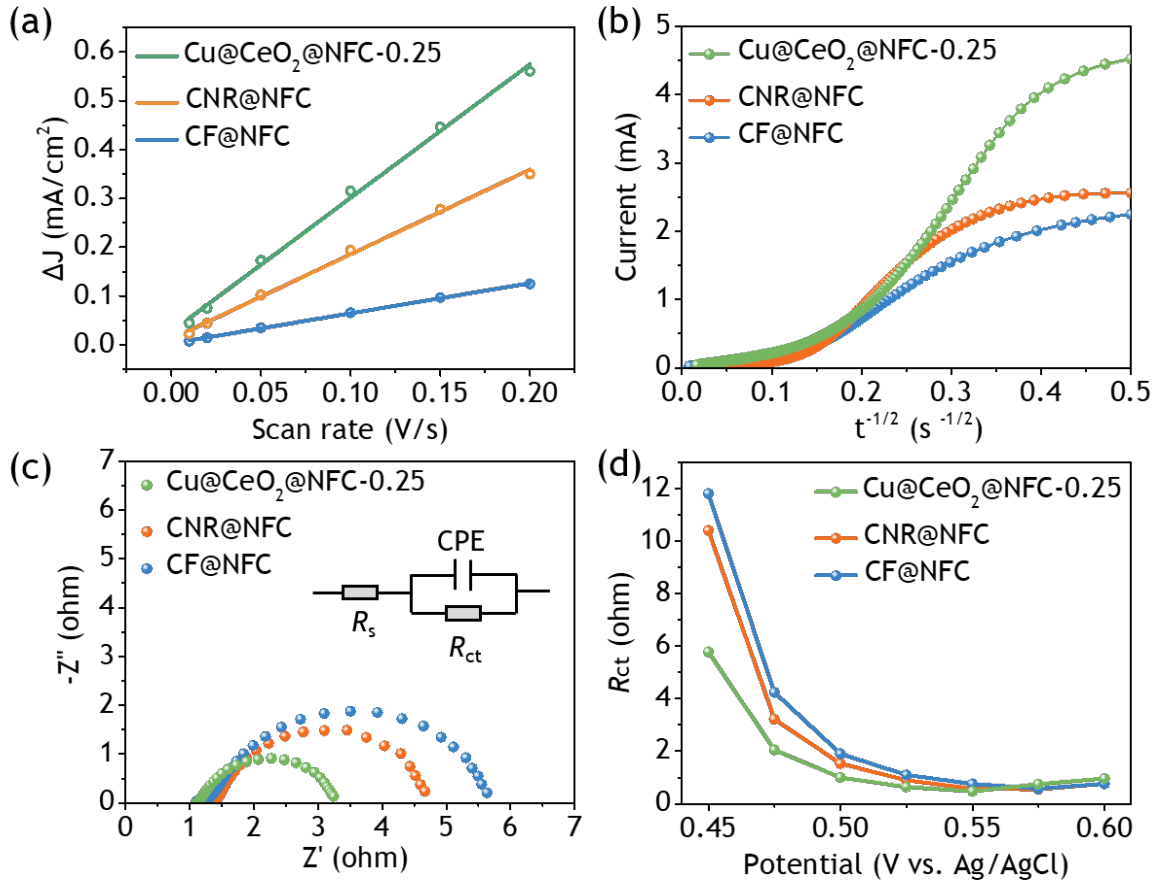

Figure 5. Electronic activities of for catalytic activity. (a) Linear fitting of the capacitive currents of different samples plotted against scan rate. (b) Chronoamperometric measurements of the oxygen diffusion rate. (c) Electrochemical impedance spectra (EIS) of different samples with an applied potential of overpotential at 10 mV/cm^2, respectively. (d) Rct of different samples with applied potential at 0.45-0.6 V vs. Ag/AgCl at a range of 0.025 V.

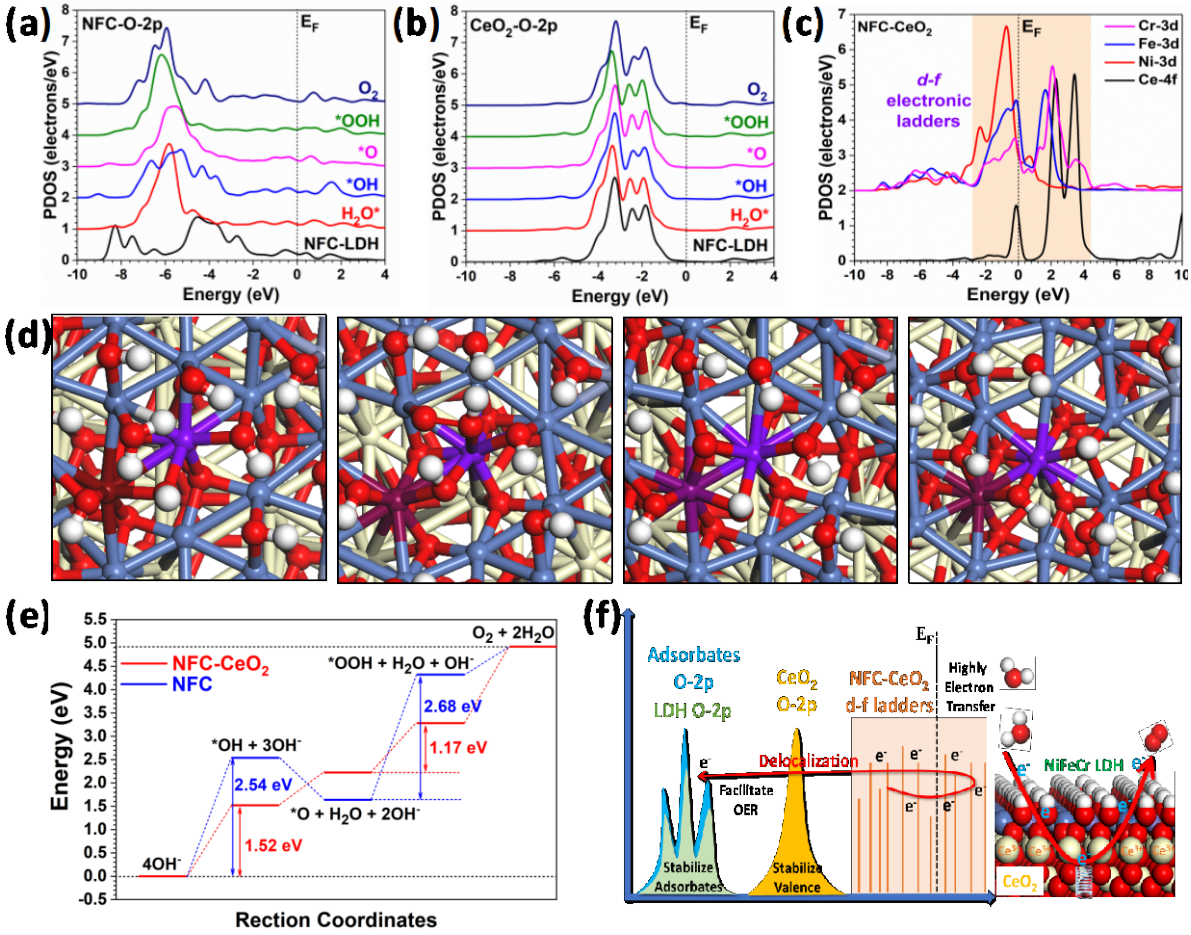

Figure 6. Electronic properties, structure configurations and energetic pathway of NFC-CeO_2 for OER. (a) The PDOS of O-2p orbitals in NFC-LDH in OER. (b) The PDOS of O-2p orbitals in CeO_2 in OER. (c) The PDOS of NFC-CeO_2. (d) The adsorption behaviours of key intermediates [H_2O*], [*OH], [*O] and [*OOH] in OER. The surface OH from NFC has been omitted for better illustration. Red Balls = O, White Balls= H, Yellow Balls = Ce, Navy Balls = Ni, Purple Balls = Fe and Brown Balls = Cr. (e) Energetic pathway of OER on NFC and NFC-CeO_2. (f) Schematic diagram of the d-f electronic ladders by NFC-CeO_2 for boosting OER.

A novel and highly efficient hybrid electrocatalyst is synthesized by NiFeCr hydroxide deposited on porous peapod-like Cu@CeO_2 nanotube array. The introduction of CeO_2 supplies abundant *d-f* orbital ladders to construct a highly efficient electron transfer expressway, leading to the superior alkaline OER performance.

Keyword: Rare-earth Oxide Electrocatalyst

Jiale Xia[+], Mingzi Sun[+], Hongyang Zhao[+], Bolong Huang*, Lingling Xu, Meng Luo, Jianwei Zhang, Feng Luo, Yaping Du*, and Chun-Hua Yan

Title Interfacial Ion-Exchange of Rare Earth Ceria (III/IV) Boosts Highly Active Oxygen Evolution Reaction